Lawrence Berkeley National Laboratory
LBL Publications

Title

Integrated rocksalt—polyanion cathodes with excess lithium and stabilized cycling

Permalink

https://escholarship.org/uc/item/9bs5g3ck

Journal

Nature Energy, 9(12)

ISSN

2058-7546

Authors

Huang, Yimeng
Dong, Yanhao
Yang, Yang
et al.

Publication Date

2024-12-01

DOI

10.1038/s41560-024-01615-6

Copyright Information

Peer reviewed

Integrated polyanion-rocksalt cathodes with excess lithium and stabilized cycling

Yimeng Huang[1], Yanhao Dong[2,*], Yang Yang[3], Tongchao Liu[4], Moonsu Yoon[5,6], Sipei Li[5], Baoming Wang[5], Yongwen Sun[3], Ying Han[3], Jim Ciston[7], Colin Ophus[7], Chengyu Song[7], Aubrey Penn[8], Jinhyuk Lee[9], Yaqi Liao[10], Haijin Ji[10], Ting Shi[10], Mengyi Liao[10], Zexiao Cheng[10], Jingwei Xiang[10], Yu Peng[11], Wei-Ren Liu[12], Rasu Muruganantham[12], Chun-Chuen Yang[13], Lu Ma[14], Xianghui Xiao[14], Yuntong Zhu[1], Qingjie Li[5], Ethan Yupeng Zheng[1], Avetik Harutyunyan[15], Ju Li[1,5,*]

[1]Department of Materials Science and Engineering, Massachusetts Institute of Technology, Cambridge, Massachusetts 02139, USA

[2]State Key Laboratory of New Ceramics and Fine Processing, School of Materials Science and Engineering, Tsinghua University, Beijing, 100084, China

[3]Department of Engineering Science and Mechanics and Materials Research Institute, The Pennsylvania State University, University Park, Pennsylvania 16802, USA

[4]Chemical Sciences and Engineering Division, Argonne National Laboratory, Argonne, IL 60439

[5]Department of Nuclear Science and Engineering, Massachusetts Institute of Technology, Cambridge, Massachusetts 02139, USA

[6]Department of Chemical & Biological Engineering, Gachon University, Seongnam-si, Gyeonggi-do 13120, Republic of Korea

[7]National Center for Electron Microscopy, Molecular Foundry, Lawrence Berkeley National Laboratory, Berkeley, CA 94720, USA

[8]MIT.Nano, Massachusetts Institute of Technology, Cambridge, Massachusetts 02139, USA

[9]Department of Mining and Materials Engineering, McGill University, Montréal, QC H3A 0C5, Canada

[10]Department of Materials Science and Engineering, Huazhong University of Science and Technology, Wuhan 430074, China

[11]Department of Chemistry, Department of Materials Science, Shanghai Key Laboratory of Molecular Catalysis and Innovative Materials, Fudan University, Shanghai 200433, China

[12]Department of Chemical Engineering, Chung Yuan Christian University, Taoyuan City 32023, Taiwan R.O.C.

[13]Department of Physics, National Central University, Taoyuan City 320317, Taiwan R.O.C.

[14]National Synchrotron Light Source II, Brookhaven National Laboratory, Upton, NY 11973, USA

[15]Honda Research Institute USA, Inc., San Jose, CA 95134, USA

*Corresponding authors. Email: dongyanhao@tsinghua.edu.cn (Y.D.), liju@mit.edu (J.L.)

Abstract

Co- and Ni-free disordered rocksalt (DRX) cathodes utilize oxygen redox to increase the energy density of lithium-ion batteries (LIBs), but it is challenging to achieve good cycle life at high voltages > 4.5 V (vs. Li/Li$^+$). Here we report a new family of Li-excess Mn-rich cathodes that integrates rocksalt- and polyanion-type structures. Guided by design rules of cation filling and ordering, bulk incorporation of polyanion groups into the rocksalt lattice has been demonstrated. The integration bridges the two most important families of LIB cathodes, i.e., layered/spinel and phosphate oxides. This dramatically enhances the cycling stability of DRX cathodes with 4.8 V upper cutoff voltage, and enables high energy densities above 1100 Wh kg^{-1} and > 70% retention over 100 cycles. This bridging opens a vast compositional space for the development of battery cathodes that use only earth-abundant elements such as Mn and Fe.

Introduction

Rapid growth of electricity storage capabilities with lithium-ion batteries (LIBs) is required to realize a sustainable energy infrastructure[1]. In terms of resources, Co is ~5× the price of Li on a molar basis[2,3], and Ni is ~2×[3], thus we would run into Co or Ni crises before Li. For advanced LIB cathodes, eliminating Co and Ni usage would greatly improve the scalability of electricity storage[4]. Disordered rocksalt (DRX) cathodes[5,6] are attractive for being potentially Co/Ni-free, while having high energy densities (approaching 1100 Wh kg^{-1} [7]). On the other hand, to reach high energy densities (> 900 Wh kg^{-1}), high upper cutoff voltages (e.g., 4.8 V vs. Li/Li$^+$ for DRX[7-11]) are required for cathodes, which means highly delithiated states with most of the Li$^+$-hosting sites vacant. This often triggers the participation of oxygen anion redox and eventually irreversible oxygen loss, as delithiation lowers the Fermi level towards or dropping below the top of the oxygen 2p band, especially at the surface and interfaces[6,12-14]. A heavy usage of hybrid anion- and cation-redox (HACR) with more exotic oxygen valence O$^{\alpha-}$ (0 < α < 2) challenges the cycling stability of the cathode since O$^{\alpha-}$ tends to be more mobile, leading to percolating lattice oxygen diffusion to the reactive surface, extensive side reactions with the electrolyte, and finally structural and chemical instability at the surface and in the bulk[15-19]. These are critical issues for DRX[6,20] and other high-energy-density cathodes[16,21].

LIB cathodes are mainly constructed on face-centered cubic (FCC) oxygen or lower-symmetry polyanion framework (HCP oxygen for LFP, the most useful polyanion cathode). The former may also have cation ordering in the parent rocksalt structure, which includes high-energy-density cathodes of LiCoO$_2$, Ni-rich layered cathodes, and Li-/Mn-rich layered cathodes[22,23]. (Spinel and DRX cathodes are also rocksalt structure derivatives with FCC oxygen sublattice.) They have high theoretical capacity > 270 mAh g^{-1}, and extensive research has been conducted to improve

their high-voltage stability. The latter is exemplified by $LiFePO_4$, with exceptional structural, electrochemical, and thermal stability, yet limited by the low theoretical capacity (170 mAh g^{-1}) and low energy density at the cathode level[24-26]. Marriage between the two families may offer synergistically improved energy density and stability. However, few reports[27] of their integration testify to the incompatibility between rocksalt and polyanion structures.

This work seeks to resolve the above conundrum with the invention of integrated rocksalt-polyanion cathodes. These new compositions originate from DRX chemistry, and a major effort here is to improve the cycling stability under high upper cutoff voltage. We successfully produced a family of Li-excess Co/Ni-free disordered rocksalt-polyanionic spinel (DRXPS) cathodes, with a general chemical formula of $Li_{2+u-v}M_{2-u}[XO_4]_xO_{4(1-x)}$. Here M denotes transition metals such as Mn and Fe, XO_4 denotes polyanion groups such as PO_4, BO_4, SiO_4, and SO_4, and u, v, and x describe the designed stoichiometries. This family of compounds is called DRXPS because they are designed on a parent DRX structure, and have bulk polyanion incorporation and spinel-type cation ordering (that gives spinel diffraction pattern). Remarkable improvements of the cycling stability over reported DRX cathodes have been achieved in $Li_{1.67}Mn_{1.5}P_{0.17}O_4$, $Li_{1.67}Mn_{1.5}B_{0.17}O_4$, $Li_{1.67}Mn_{1.25}Fe_{0.25}P_{0.17}O_4$, and four more compositions, all belonging to the DRXPS family. The new DRXPS cathodes have high capacities (> 350 mAh g^{-1}), high energy densities (> 1100 Wh kg^{-1}), stable cycling (> 70% energy density retention after 100 cycles), good rate performance, and a highly tunable compositional space. The general design principles and experimental efforts presented here offer new avenues for the future development of Co,Ni-free cathodes.

Materials design

Our task is to design high-capacity oxide cathodes with excess Li, anion redox activity, bulk polyanion incorporation and good electrochemical stability. Starting from the high-capacity FCC oxygen framework, three-dimensionally connected spinel structure M_2O_4 (**Figure 1a**, Li is not shown for simplicity) provides the best hybridization between transition metal (M) d and oxygen $2p$ orbitals under the constrained Li/M ratio of 1. (Each oxygen is coordinated with one tetrahedral Li and three octahedral M.) Further raising the Li/M ratio above 1 (i.e., replacing some M in **Figure 1a** by Li) increases the theoretical capacity and anion redox is simultaneously activated with underbonded oxygen (**Figure 1b**). These underbonded oxygen can be oxidized upon charging to high voltages and may eventually leave the lattice in the form of outgassing if a percolative kinetic pathway exists from the bulk to the surface[28]. We aim to shut down the labile oxygen percolation by incorporating some polyanion groups in the Li-excess lattice (**Figure 1c**) and utilizing the strong X-O covalent bonds to mitigate oxygen instability.

Practical realization of the above is challenging and comes to the same incompatibility issue between rocksalt

and polyanion structures discussed above. The main reasons are two-fold. First, the cations in polyanion cathodes are not close-packed. The octahedral sites face-shared with XO_4 tetrahedral need to be empty[24]. This conflicts with cation-filling rules in layered and DRX cathodes (the octahedral sites are fully occupied). Second, X-O covalent bonds are short and strong, which results in much shorter O-O distances (characterizing the tetrahedral size) than the ones in rocksalt-structure cathodes. For example, the true tetrahedra size calculated from the P-O bond length in polyanion olivine cathode $LiFePO_4$[29,30] is 12–15% smaller than that in rocksalt-structure cathodes[31-34] (**Figure 1d**). This would result in large lattice distortion and thus, difficulty in making a solid-solution phase between XO_4 polyanions and "normal O" anions.

We proposed the following solution to the two problems above. For the first one, cation deficiency is clearly the best approach. Specifically, we were inspired by the polyhedral occupation rules in spinel cathodes: octahedra at 16d sites are fully occupied, and octahedra at 16c sites (face-shared with tetrahedra at 8a sites) are empty. So spinel-like cation ordering is preferred. For the second one, typical high-temperature solid-state synthesis would not work, and we resort to lower-temperature mechano-chemical synthesis. Without going into the detailed derivations of the optimal values of stoichiometry (u, v, and x) in **Supplementary Note S1**, we show in the following sections that the above simple design rules are powerful enough to guide the synthesis of the DRXPS cathode series.
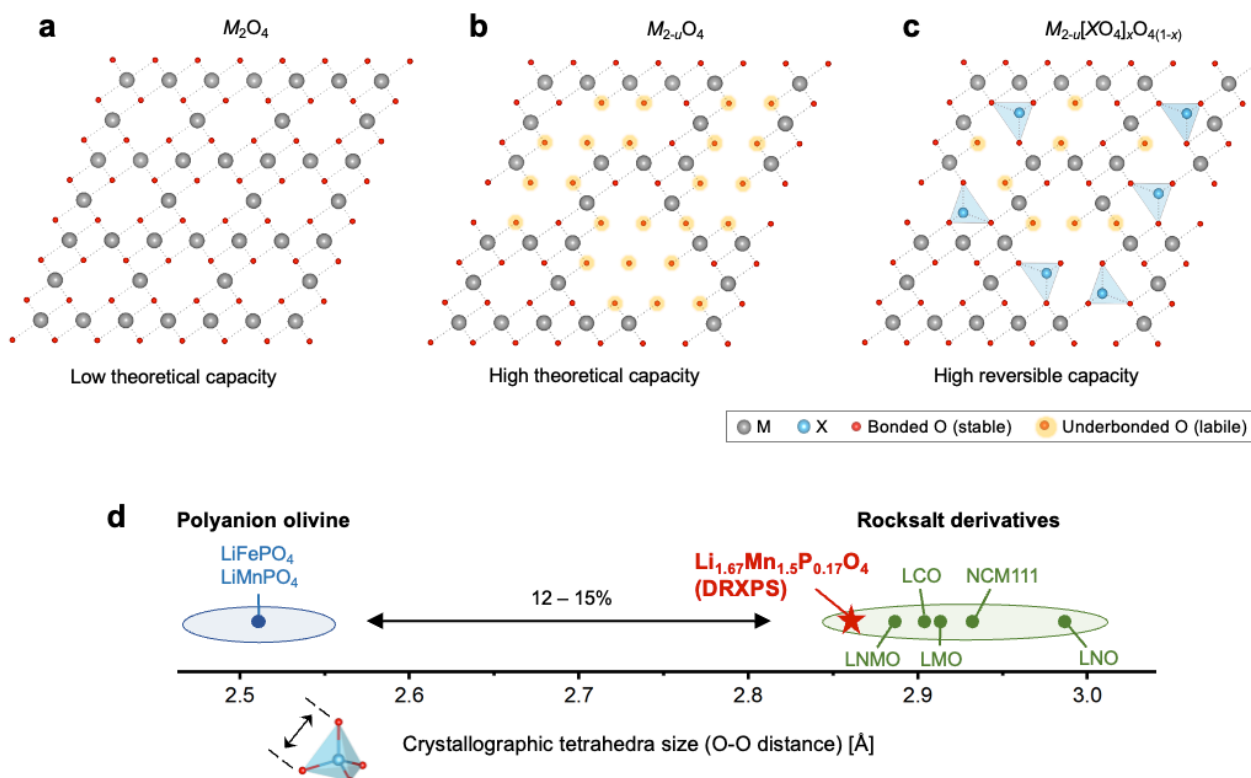

Fig. 1 | Design of DRXPS cathodes. a, Structure of M_2O_4. **b,** Structure of $M_{2-u}O_4$. **c,** Structure of $M_{2-u}[XO_4]_xO_{4(1-x)}$. **d,**

Comparison of crystallographic tetrahedra size for polyanion olivine and rocksalt-type cathodes. LMO: $LiMn_2O_4$, LNMO: $LiNi_{0.5}Mn_{1.5}O_4$, LCO: $LiCoO_2$, NCM111: $LiNi_{1/3}Co_{1/3}Mn_{1/3}O_2$, LNO: $LiNiO_2$.

Structure and morphology of prototype $Li_{1.67}Mn_{1.5}P_{0.17}O_4$

A prototype DRXPS cathode $Li_{1.67}Mn_{1.5}P_{0.17}O_4$ was synthesized by a one-pot mechanochemical method. The obtained sample has a composition close to the designed stoichiometry (shown by inductively coupled plasma mass spectrometry, ICP-MS, data in **Supplementary Table S1**). Its X-ray diffraction (XRD) pattern (**Figure 2a**) matches with a single-phase cubic spinel structure ($a=b=c$, $\alpha=\beta=\gamma=90^o$, **Supplementary Figure S1**). Rietveld refinement yields a lattice constant $a = 8.1527$ Å (**Supplementary Figure S1** and **Supplementary Table S2**), which is slightly smaller than those of spinel cathodes (8.246 Å for $LiMn_2O_4$ and 8.172 Å for $LiNi_{0.5}Mn_{1.5}O_4$). For more structural information, we conducted pair distribution function (PDF) analysis on $Li_{1.67}Mn_{1.5}P_{0.17}O_4$ (**Figure 2b**), and compared with references of $LiMn_2O_4$ and $LiFePO_4$ (**Supplementary Figure S2**). First-nearest-neighbor P-O pair at 1.549 Å was observed, which is slightly longer than the P-O pair in the PO_4 group of $LiFePO_4$ (1.520 Å). First-nearest-neighbor Mn-O pair at 1.893 Å and Mn-Mn pair 2.858 Å were observed, which are slightly shorter than the corresponding ones in $LiMn_2O_4$ (1.903 Å for Mn-O and 2.887 Å for Mn-Mn). These elastic straining effects are consistent with our materials design (tensile strained for XO_4 compared to $LiFePO_4$ and compressive strained for MO_6 compared to $LiMn_2O_4$). The effect smears at longer distances, e.g., second-nearest-neighbor Mn-O distances (3.418 Å) are similar in $Li_{1.67}Mn_{1.5}P_{0.17}O_4$ and $LiMn_2O_4$. Raman spectroscopy measurement (**Supplementary Figure S3**) was conducted for local structure analysis. The Raman peak at ~940 cm^{-1} can be assigned to the A_{1g} mode of PO_4[35], the peak at ~600 cm^{-1} can be assigned to the symmetric stretching mode of MnO_6[36,37], and the peaks at 420 – 490 cm^{-1} can be assigned to the symmetric stretching modes of LiO_4 and LiO_6[36]. These Raman features support tetrahedral occupation of P, octahedral occupation of Mn, and mixed tetrahedral/octahedral occupations of Li.

Scanning electron microscopy (SEM) image in **Figure 2c** shows that $Li_{1.67}Mn_{1.5}P_{0.17}O_4$ has a particle size of ~200 nm. Elemental dispersive spectroscopy (EDS) mapping (**Figure 2d**) shows a uniform distribution of Mn, P, and O. Transmission electron microscopy (TEM) image in **Figure 2e** shows that the particles in **Figure 2c** are polycrystalline, consisting of 5-10 nm "primary" particles which are crystalline. A characteristic lattice spacing $d = 4.69$ Å can be identified, corresponding to the (111) plane of the spinel structure. The selected area electron diffraction (SAED) pattern (inset of **Figure 2e**) further confirms the polycrystallinity, with diffraction rings corresponding to the (111), (311), (400), (511) and (440) peaks. **Figure 2f** shows the electron energy loss spectroscopy (EELS) mapping of a $Li_{1.67}Mn_{1.5}P_{0.17}O_4$ primary particle, with uniform Mn, P, and O distributions, in support of bulk incorporation of

P in the lattice. (Additional support from energy dispersive X-ray spectroscopy, EDS, is shown in **Supplementary Figure S4**.)

With the above information, we constructed the structural model (**Figure 2g**). Per chemical formula $Li_{1.67}Mn_{1.5}P_{0.17}O_4$, 4 O at 32e sites forms the FCC anion framework, 1.5 Mn occupy 3/4 of the 16d cation octahedral sites, and 0.17 P occupy 1/6 of the 8a cation tetrahedral sites. As 16d sites should be fully occupied in spinel structure, the remaining 1/4 should be occupied by 0.5 Li. This leaves 1.17 Li that occupy either 8a or 16c sites. Therefore, using □ to denote cation vacancy (i.e., unoccupied tetrahedral/octahedral sites), we can write the structural model as $(P_{0.17}Li_t\square_{0.83-t})_{8a}(Li_{1.17-t}\square_{0.83+t})_{16c}(Li_{0.5}Mn_{1.5})_{16d}(O_4)_{32e}$. The calculated XRD pattern from the constructed structure (black solid curve in **Figure 2a**) matches well with the experimental one, and it is close to the refined structure (**Supplementary Table S2**). The proposed structural model is further supported by high-angle annular dark field scanning transmission electron microscopy (HAADF-STEM) image in **Figure 2h**. Spinel-type cation ordering with Mn atoms at 16d octahedral sites, viewed along the [110] zone axis, is clearly shown. The alternating intensities at 16d sites (brighter at Mn1 sites and darker at Mn2 sites; schematics shown in the inset of **Figure 2h**) is also a characteristic feature of the spinel structure[38,39]. Further analysis using a least absolute shrinkage and selection operator (LASSO) filter (see Methods) was applied to obtain **Figure 2i**. In addition to 16d site signals, some intensities are present at 8a sites (see top-left and bottom-right insets of **Figure 2i**). These 8a site signals are attributed to P only, as Li has no contrast under the HAADF mode and it is difficult for Mn to enter tetrahedral sites.
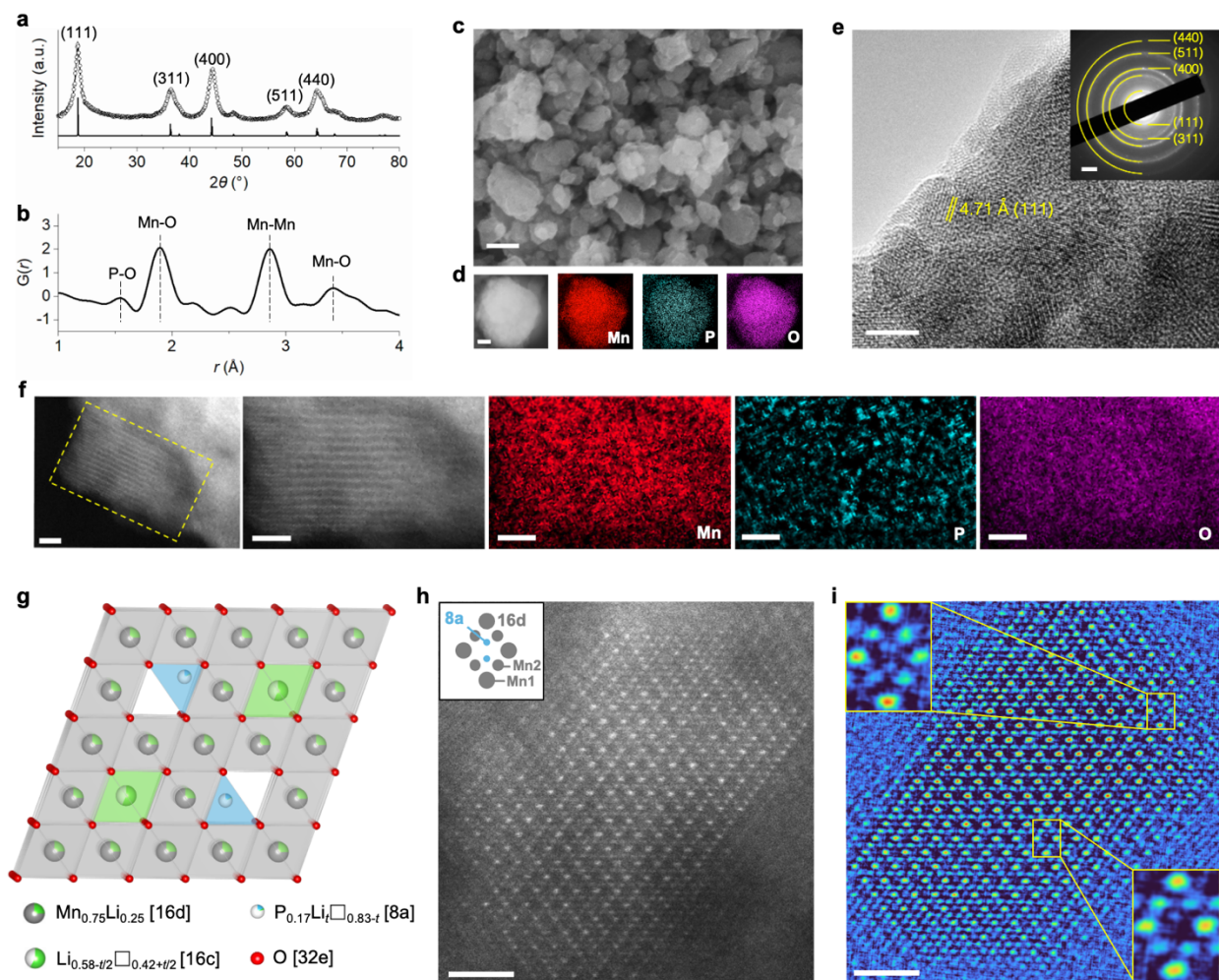
Fig. 2 | Design and structural characterization of $Li_{1.67}Mn_{1.5}P_{0.17}O_4$. a, XRD patterns of $Li_{1.67}Mn_{1.5}P_{0.17}O_4$ (black open circles are experimental and black solid line is calculated). **b,** Pair distribution function of $Li_{1.67}Mn_{1.5}P_{0.17}O_4$. **c,** SEM image of $Li_{1.67}Mn_{1.5}P_{0.17}O_4$. Scale bar, 200 nm. **d,** STEM-EDS mapping of $Li_{1.67}Mn_{1.5}P_{0.17}O_4$. Scale bar, 100 nm. **e,** TEM image of $Li_{1.67}Mn_{1.5}P_{0.17}O_4$. Scale bar, 5 nm. Inset: SAED pattern. Scale bar, 2 nm^{-1}. **f,** STEM-EELS mapping of Mn, P and O performed on a single crystal grain close to a zone axis. Scale bar, 2 nm. **g,** Structural model of $Li_{1.67}Mn_{1.5}P_{0.17}O_4$. **h,** HAADF-STEM image of $Li_{1.67}Mn_{1.5}P_{0.17}O_4$. Scale bar, 1 nm. **i,** Filtered image of (h). Scale bar, 1 nm.

Electrochemistry and redox mechanism of $Li_{1.67}Mn_{1.5}P_{0.17}O_4$

We first evaluated the electrochemical performance of $Li_{1.67}Mn_{1.5}P_{0.17}O_4$ in coin-type half cells between $1.5 - 4.8$ V vs. Li/Li^+ at room temperature. **Figure 3a** shows the galvanostatic charge-discharge curves of the first two cycles at 20 mA g^{-1}, with high discharge capacities of ~365 mAh g^{-1} and high discharge energy densities of ~1120 Wh kg^{-1}. Converting the capacity to stoichiometry, we estimated a high Li usage of 1.63 Li removal (out of 1.67 Li) per formula

unit (**Figure 3b**) in the first charge. Since Mn in $Li_{1.67}Mn_{1.5}P_{0.17}O_4$ has an average valence of +3.67 (slightly lower Mn average valence may be possible depending on synthesis conditions) and Mn^{3+}/Mn^{4+} can only charge-compensate for 0.5 Li removal, we expect active participation of anion redox $O^{2-}/O^{\alpha-}$ ($0 < \alpha < 2$). During the first discharge, 2.23 Li was inserted into the structure, ending with an over-lithiated composition of $Li_{2.27}Mn_{1.5}P_{0.17}O_4$. The over-lithiation should be charge-compensated by Mn reduction. The second cycle shows a similar discharge curve to the first one, indicating good reversibility.

To better understand the redox mechanism, we performed ex situ hard X-ray absorption spectroscopy. **Figure 3c** shows the Mn K-edge X-ray absorption near-edge structure (XANES) for $Li_{1.67}Mn_{1.5}P_{0.17}O_4$ at different states of charge (marked on the voltage profiles in **Supplementary Figure S5b**). Since the near-edge structure depends on both the oxidation state and the bonding environment[40], we analyzed Mn valence by comparing with reference spectra (**Supplementary Fig. S5a**). For the first two cycles, all Mn K-edge spectra stay higher in energy than the Mn_2O_3 (Mn^{3+}) reference, and shift to higher energy (Mn oxidation) during charge and to lower energy (Mn reduction) during discharge, indicating active participation of reversible $Mn^{3+/4+}$ redox couple. For charge in the first (Pristine to 1Ch-4.8V) and second cycle (1DCh-1.5V to 2Ch-4.8V), capacities of 269 and 384 mAh g^{-1} are observed (corresponding to Mn valence changes of +1.09 and +1.56), respectively. Meanwhile, Mn K-edges for both charge half-cycles shift from between the Mn_2O_3 (Mn^{3+}) and MnO_2 (Mn^{4+}) reference spectra to close to MnO_2 (Mn^{4+}). Such a one-electron TM redox cannot account for the high reversible capacity by itself. For discharge to 3.5 V vs. Li/Li$^+$ (1Ch-4.8V to 1DCh-3.5V and 2Ch-4.8V to 2DCh-3.5V), a capacity of ~96 mAh g^{-1} (corresponding to a Mn valence change of –0.39) are observed for both cycles, while the Mn K-edges for both only experience minor downshifts. Therefore, active oxygen redox should also be involved during charge to 4.8 V vs. Li/Li$^+$ and discharge to 3.5 V vs. Li/Li$^+$ for the initial two cycles. Capacities below 3.5 V vs. Li/Li$^+$ should be solely contributed by the $Mn^{3+/4+}$ redox couple since the Mn K-edges lie between the Mn_2O_3 (Mn^{3+}) and MnO_2 (Mn^{4+}) spectra, and the shifts roughly match the expected Mn valence change (converted from the observed capacity).

The rate performance of $Li_{1.67}Mn_{1.5}P_{0.17}O_4$ was tested from 20 mA g^{-1} to 1000 mA g^{-1} (~5.5 C calculated from the charging time). Capacity retentions of 75% and 51% were observed when the galvanostatic current density increased from 20 mA g^{-1} to 200 mA g^{-1} and 1000 mA g^{-1}, respectively (**Figure 3d**). The cycling performance of $Li_{1.67}Mn_{1.5}P_{0.17}O_4$ was tested at 50 mA g^{-1} between 1.5 – 4.8 V vs. Li/Li$^+$, after two formation cycles at 20 mA g^{-1}. After 100 cycles, it has a capacity retention of 72% (upper panel of **Figure 3e**), an average discharge voltage maintained at > 3 V vs. Li/Li$^+$ (minimal voltage decay of < 7.4 mV per cycle, lower panel of **Figure 3e**), and a discharge energy retention of 71% (**Supplementary Figure S6**). For comparison, we tested the cycling performance

of similarly synthesized polyanion-free $Li_{1.67}Mn_{1.5}Nb_{0.17}O_4$ and $Li_{1.93}Mn_{1.65}O_4$ as control groups (**Supplementary Figure S7**; both have spinel-like structures, and an average Mn valence of +3.67, similar to $Li_{1.67}Mn_{1.5}P_{0.17}O_4$). Shown in **Figure 3e**, $Li_{1.67}Mn_{1.5}Nb_{0.17}O_4/Li_{1.93}Mn_{1.65}O_4$ show faster degradations with 45%/27% capacity retention, and 44%/25% energy density retention after 100 cycles under the same testing conditions. Remarkably, $Li_{1.67}Mn_{1.5}P_{0.17}O_4$ have suppressed gas evolution (in situ differential electrochemical mass spectrometry, DEMS, in **Supplementary Figure S8**), Mn dissolution in the electrolyte (**Supplementary Figure S9a**), and Mn deposition on the anode (**Supplementary Figure S9b**) compared to $Li_{1.67}Mn_{1.5}Nb_{0.17}O_4$, all indicating stability enhancement in the former composition. (More detailed comparisons between $Li_{1.67}Mn_{1.5}P_{0.17}O_4$ and $Li_{1.67}Mn_{1.5}Nb_{0.17}O_4$ are provided in **Supplementary Note S2**.) The high-voltage cycling stability of $Li_{1.67}Mn_{1.5}P_{0.17}O_4$ is much superior over the DRX cathodes reported in the literature (see comparison in **Supplementary Table S3 and Supplementary Figure S10**). Lastly, to evaluate the electrochemical performance of $Li_{1.67}Mn_{1.5}P_{0.17}O_4$ under more practically relevant conditions, we assembled $Li_{1.67}Mn_{1.5}P_{0.17}O_4$|Li metal anode pouch cells. A good capacity retention of 74% and stable discharge voltage around 3.11 V (**Figure 3g**, with no voltage decay) have been achieved over 50 cycles at 50 mA g^{-1} between 1.5 – 4.8 V.
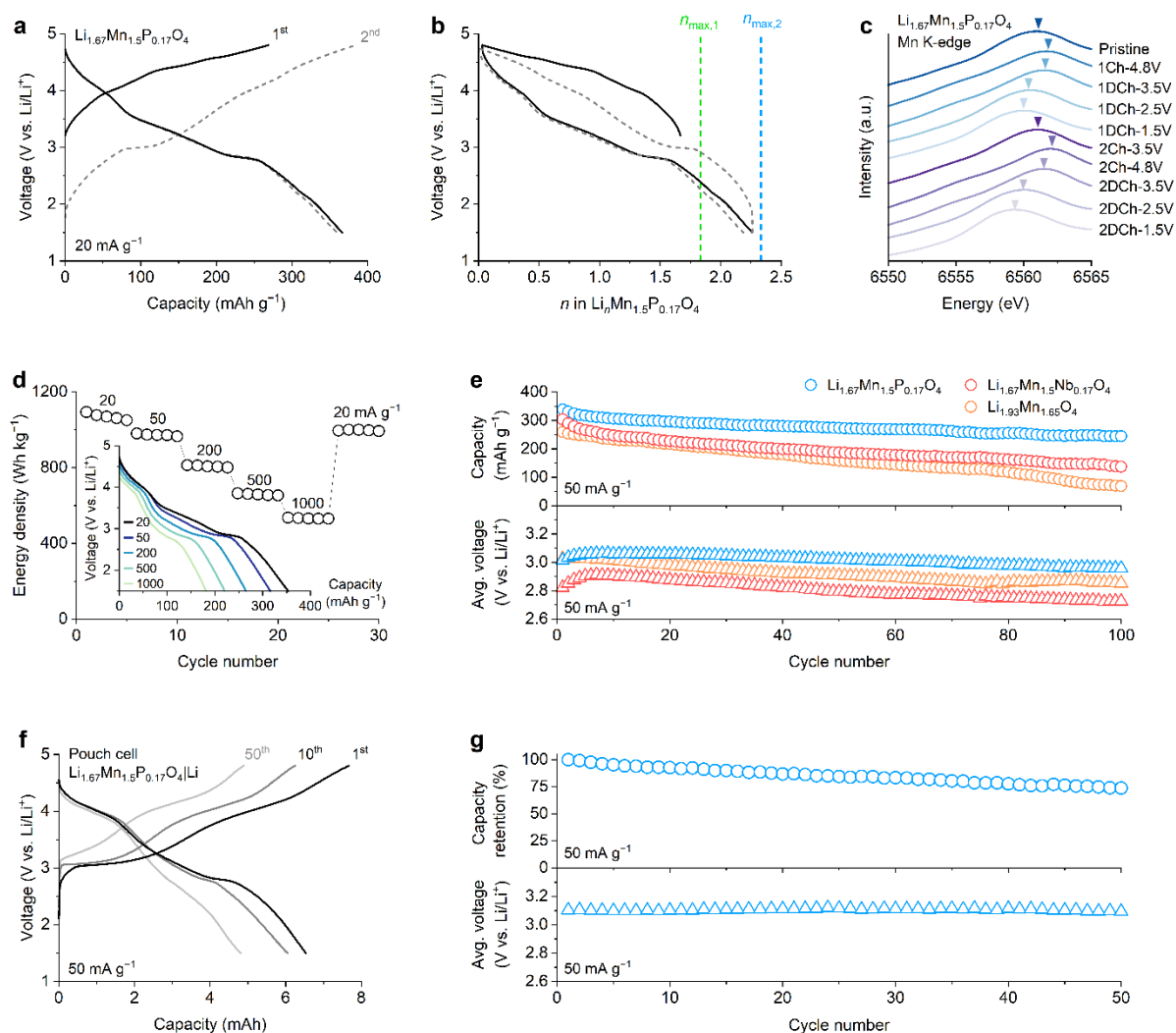
Fig. 3 | Electrochemistry and redox mechanism of $Li_{1.67}Mn_{1.5}P_{0.17}O_4$. a, Voltage profiles of $Li_{1.67}Mn_{1.5}P_{0.17}O_4$ in the initial two formation cycles between 1.5 – 4.8 V vs. Li/Li^+ at 20 mA g^{-1}. **b,** Capacity from (**a**) converted to Li content n. The theoretical capacity is marked by the dashed lines under two assumptions: if Li tetrahedral occupation is not allowed (green dashed line); if Li tetrahedral occupation is allowed (blue dashed line). **c,** Mn K-edge XANES spectra of $Li_{1.67}Mn_{1.5}P_{0.17}O_4$ in the first two cycles. **d,** Rate performance test of $Li_{1.67}Mn_{1.5}P_{0.17}O_4$ under at 20, 50, 200, 500 and 1000 mA g^{-1} (the same cell was used). Inset: Voltage profiles of the first cycle at 20, 50, 200, 500 and 1000 mA g^{-1}. **e,** Discharge capacity (top) and average discharge voltage (bottom) retention of $Li_{1.67}Mn_{1.5}P_{0.17}O_4$, $Li_{1.67}Mn_{1.5}Nb_{0.17}O_4$ and $Li_{1.93}Mn_{1.65}O_4$ in 100 cycles between 1.5 – 4.8 V vs. Li/Li^+ at 50 mA g^{-1}, following the two initial formation cycles at 20 mA g^{-1} (not shown). **f,** Voltage profiles of ($Li_{1.67}Mn_{1.5}P_{0.17}O_4$ | Li) pouch cell at the 1st, 10th and 50th cycle between 1.5 – 4.8 V vs. Li/Li^+ at 50 mA g^{-1} (following two formation cycles at 20 mA g^{-1}). **g,** Discharge capacity (top) and average discharge voltage (bottom) retention of the pouch cell during 50 mA g^{-1} cycling.

Exploring compositional space of DRXPS

The DRXPS family has a rich chemistry. To demonstrate, we show the following examples within the general formula $Li_{2+u-v}M_{2-u}[XO_4]_xO_{4(1-x)}$. We first varied the P content in $Li_{1.67}Mn_{1.67-x}P_xO_4$ ($0 \leq x \leq 0.5$, **Supplementary Figure S11a**). The XRD patterns of the four synthesized compounds are shown in **Figure 4a** (more examples in **Supplementary Figure S11a**). Phase-pure spinel structure readily forms at $x \leq 0.27$, while the impurity phase begins to form at $x \geq 0.33$ (from unreacted MnO_2 precursor). To evaluate the electrochemical performance, we cycled $Li_{1.67}Mn_{1.67-x}P_xO_4$ at 50 mA g^{-1} between 1.5 – 4.8 V vs. Li/Li$^+$, after two formation cycles at 20 mA g^{-1}. **Figure 4b** shows the voltage profiles of the four selected compositions in the initial two formation cycles. As shown in **Figure 4c** and **Supplementary Figure S11b**, PO$_4$ incorporation drastically improves the cycling stability over P-free $Li_{1.67}Mn_{1.67}O_4$. For better quantifications, we compared the discharge energy density at the 25th cycle at 50 mA g^{-1} (**Supplementary Figure S11c**) and benchmarked against 730 Wh kg^{-1} reported by Ji *et al.*[7] for DRX and related cathodes. We found that the relation between x and cycling performance resembles that of a volcano plot (also true at the 100th cycle, see **Supplementary Figure S11d**), and $0.13 \leq x \leq 0.23$ offers stabilized energy density of 867-890 Wh kg^{-1} at the 25th cycle. The experimentally observed volcano plot behavior and x range are quantitatively consistent with analytical derivations ($0.159 \leq x \leq 0.222$ in **Supplementary Note S1**) based on our stated design principles. (A detailed study of the compositions with varying u and v is provided in **Supplementary Note S3**.)

We next practiced Mn-Fe substitution. Fe is another redox-active and earth-abundant element that attracts continuous interest. $Li_{1.67}Mn_{1.25}Fe_{0.25}P_{0.17}O_4$ was synthesized mechanochemically. The XRD pattern shows a single-phase cubic spinel structure (**Figure 4d**, $a=b=c=8.129$ Å, $\alpha=\beta=\gamma=90^o$). Under SEM, we confirmed that $Li_{1.67}Mn_{1.25}Fe_{0.25}P_{0.17}O_4$ consisted of polycrystalline particles (~200 nm, **Supplementary Figure S12a**) with uniform elemental distributions (EDS mapping in **Supplementary Figure S12b**), and fine primary nano particles (TEM in **Supplementary Figure S12c**; a characteristic lattice spacing of 4.69 Å, corresponding to the (111) peak of the spinel structure, and SAED in the inset of **Supplementary Figure S12c** showing polycrystalline diffraction rings that also match the phase). The electrochemical performance of $Li_{1.67}Mn_{1.25}Fe_{0.25}P_{0.17}O_4$ was tested between 1.5 – 4.8 V vs. Li/Li$^+$ at room temperature. In the first cycle at 20 mA g^{-1} (**Figure 4e**), it shows a discharge capacity of 327 mAh g^{-1} and a discharge energy density of 978 Wh kg^{-1}, which are slightly lower than the corresponding values for $Li_{1.67}Mn_{1.5}P_{0.17}O_4$. $Li_{1.67}Mn_{1.25}Fe_{0.25}P_{0.17}O_4$ shows exceptional cycling performance, with 72% capacity retention (**Figure 4f**) and 67% energy density retention (**Supplementary Figure S13b**) over 100 cycles at 50 mA g^{-1}. The substitution was extended to a higher Fe ratio to produce $Li_{1.67}MnFe_{0.5}P_{0.17}O_4$ and with some Ni to produce $Li_{1.67}Mn_{1.33}Ni_{0.17}P_{0.17}O_4$. Spinel phase has been identified for all these compositions (**Supplementary Figure S13a**).

Their cycling performances are compared with $Li_{1.67}Mn_{1.5}P_{0.17}O_4$ and $Li_{1.67}Mn_{1.25}Fe_{0.25}P_{0.17}O_4$ in **Supplementary Figure S13b**. Discharge energy densities of 610-825 Wh kg^{-1} were obtained at the 25th cycle (**Supplementary Figure S13c**), which demonstrates highly tunable TM chemistries in DRXPS.

We lastly studied different polyanion groups. In addition to valence +5 P, we mechanochemically synthesized $Li_{1.67}Mn_{1.5}X_{0.17}O_4$ with X = +3 B, +4 Si, and +6 S. These non-metallic elements all form strong covalent bonds with oxygen and adopt tetrahedral occupancy (i.e., forming XO_4 groups). As shown by the XRD patterns in **Figure 4d**, phase-pure spinel structures have been identified for $Li_{1.67}Mn_{1.5}B_{0.17}O_4$ and $Li_{1.67}Mn_{1.5}Si_{0.17}O_4$, while minor impurity peaks matching MnO_2 (precursor) exists in $Li_{1.67}Mn_{1.5}S_{0.17}O_4$ in addition to the main spinel phase. Microscopy characterizations in **Supplementary Figure S12d-f** of a selected composition, $Li_{1.67}Mn_{1.5}B_{0.17}O_4$, show a polycrystalline particle morphology with ultrafine primary ones that are well crystalized. The electrochemical performance of $Li_{1.67}Mn_{1.5}X_{0.17}O_4$ was tested between 1.5 – 4.8 V vs. Li/Li$^+$ at room temperature. **Figure 4e** shows the galvanostatic charge-discharge curves of the first two cycles at 20 mA g^{-1} for $Li_{1.67}Mn_{1.5}B_{0.17}O_4$, $Li_{1.67}Mn_{1.5}Si_{0.17}O_4$, and $Li_{1.67}Mn_{1.5}S_{0.17}O_4$. Among the three compositions, $Li_{1.67}Mn_{1.5}B_{0.17}O_4$ has the highest discharge capacity of ~360 mAh g^{-1} and the highest discharge energy density of ~1070 Wh kg^{-1}, which are comparable with the corresponding values of $Li_{1.67}Mn_{1.5}P_{0.17}O_4$. When cycled at a higher rate of 50 mA g^{-1}, good cycling stability can be identified and the discharge capacity (**Figure 4f**) and energy density (**Supplementary Figure S14**) at the 25th cycle (after two formation cycles) follows the rank of $Li_{1.67}Mn_{1.5}P_{0.17}O_4$ > $Li_{1.67}Mn_{1.5}B_{0.17}O_4$ > $Li_{1.67}Mn_{1.5}S_{0.17}O_4$ > $Li_{1.67}Mn_{1.5}Si_{0.17}O_4$. Remarkably, all these compositions show great improvements over the polyanion-free compositions (e.g., $Li_{1.67}Mn_{1.67}Nb_{0.17}O_4$ and $Li_{1.93}Mn_{1.65}O_4$). Therefore, we conclude that the integrated rocksalt-polyanion structure presented in this work is a general methodology to improve the stability of high-energy-density oxide cathodes, especially for DRX cathodes.
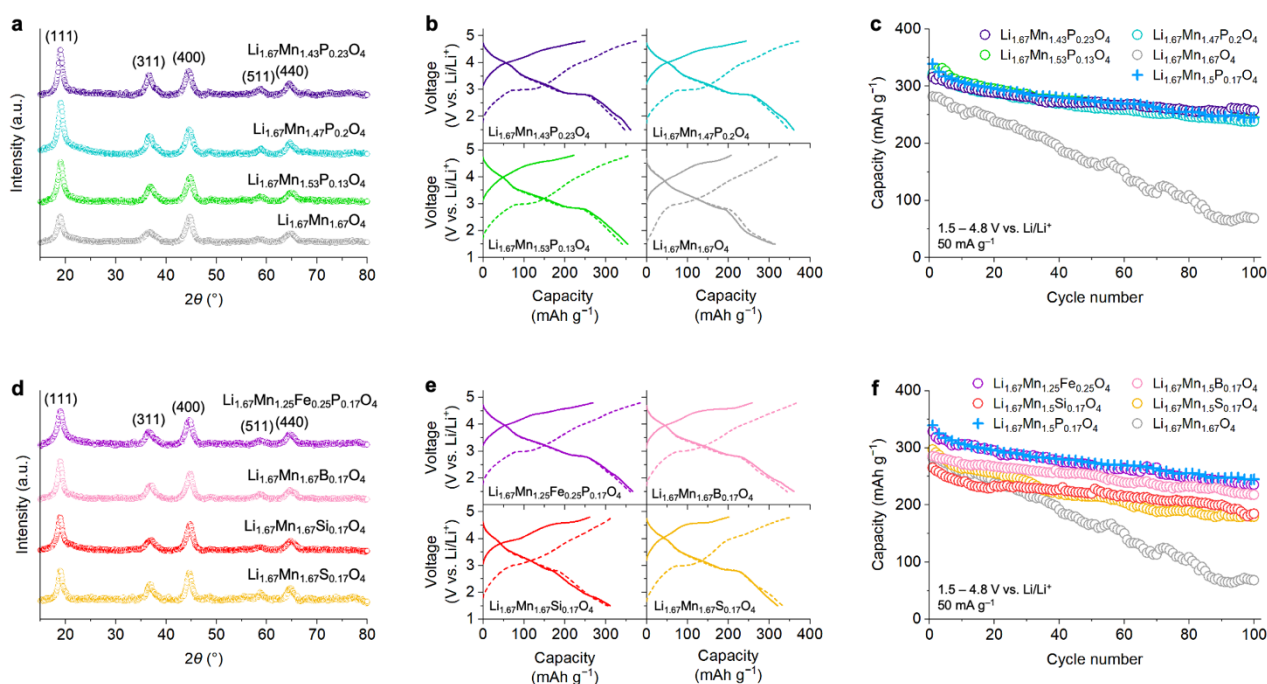
Fig. 4 | Structure and performance of diverse compositions of DRXPS. a, XRD patterns of $Li_{1.67}Mn_{1.67-x}P_xO_4$ ($x = 0$, 0.13, 0.2, 0.23). **b,** Voltage profiles of the initial two formation cycles of $Li_{1.67}Mn_{1.67-x}P_xO_4$ ($x = 0$, 0.13, 0.2, 0.23) between 1.5 – 4.8 V vs. Li/Li$^+$ at 20 mA g^{-1}. **c,** Discharge capacity of $Li_{1.67}Mn_{1.67-x}P_xO_4$ ($x = 0$, 0.13, 0.17, 0.2, 0.23) in the first 100 cycles, between 1.5 – 4.8 V vs. Li/Li$^+$ at 50 mA g^{-1}, after two formation cycles at 20 mA g^{-1} (not shown). **d,** XRD patterns of $Li_{1.67}Mn_{1.25}Fe_{0.25}P_{0.17}O_4$ and $Li_{1.67}Mn_{1.5}X_{0.17}O_4$ (X = B, Si, S). **e,** Voltage profiles of the initial two formation cycles of $Li_{1.67}Mn_{1.25}Fe_{0.25}P_{0.17}O_4$ and $Li_{1.67}Mn_{1.5}X_{0.17}O_4$ (X = B, Si, S) between 1.5 – 4.8 V vs. Li/Li$^+$ at 20 mA g^{-1}. **f,** Discharge capacity of $Li_{1.67}Mn_{1.25}Fe_{0.25}P_{0.17}O_4$ and $Li_{1.67}Mn_{1.5}X_{0.17}O_4$ (X = B, Si, S) in the first 100 cycles, between 1.5 – 4.8 V vs. Li/Li$^+$ at 50 mA g^{-1}, after two formation cycles at 20 mA g^{-1} (not shown). Data for $Li_{1.67}Mn_{1.5}P_{0.17}O_4$ and $Li_{1.67}Mn_{1.67}O_4$ are also shown for reference.

Outlook for DRXPS cathodes

To conclude, we demonstrated a promising family of Co/Ni-free DRXPS cathodes with stabilized high HACR capacities and energy densities. It overcomes the key bottleneck of poor high-voltage cyclability for the development of DRX cathodes and their derivatives. Despite the encouraging results, there remain issues to be addressed to enable the practical use of DRXPS cathodes. First, the ratio of the active materials in the composite cathode needs to be increased to > 90 wt%, while the ratio of the conductive carbon needs to be significantly lowered for better practicality (e.g., increase volumetric energy density, calculated in **Supplementary Table S4**). This can be resolved with a thin layer of uniform carbon coating, as is the case for LiFePO$_4$, which can improve the long-range electron percolation

13

in the composite electrode. Second, the cycling stability needs to be further improved to allow for > 500-1000 deep-charge/discharge cycles. This can be resolved by applying coatings, minor lattice doping, concentration-gradient design, and advanced electrolytes and electrolyte additives. With the above issues addressed, scalable synthesis methods should be developed, and DRXPS cathodes should be evaluated in practical full cells (supported by pre-lithiation technologies for the first-cycle overlithiation). We look forward to rapid progress in developing DRXPS Co,Ni-free cathodes and their practical applications in sustainable energy.

Methods

Synthesis

All compositions were synthesized using a one-pot low-temperature mechanochemical synthesis method. Li_2O, Mn_2O_3, MnO_2, Li_3PO_4, Fe_2O_3, B_2O_3, Li_2SO_4 and SiO_2 (all from Sigma-Aldrich, 99% purity) precursors were directly mixed using the Fritsch Pulverisette 7 Premium Line planetary ball mill, according to stoichiometry (e.g., $Li_{1.67}Mn_{1.5}P_{0.17}O_4 = 0.58\,Li_2O + 0.25\,Mn_2O_3 + MnO_2 + 0.17\,Li_3PO_4$). Precursor powders with a total weight of around 5 g were put into an 80 ml stainless steel jar, with 25 10-mm-diameter stainless steel balls (the weight ratio of powders to balls was 1:20), and mixed in air under 800 rpm for 5 hours. No additional heat treatment was involved.

Materials characterizations

ICP-MS was conducted on Agilent 730. ICP-OES was conducted on Agilent 5100 VDV. HRXRD data were collected at Beamline 11-BM in the 2θ range of 0.5–50° with a step size of 0.001°, counting time of 0.1 s per step, and a wavelength of λ = 0.458961 Å at 295 K and λ = 0.458956 Å at 100 K. Fine-ground polycrystalline powders were loaded into a ϕ0.8-mm Kapton capillary for installation on a magnetic sample base used by the beamline sample changer. The sample was spun continuously at 5600 rpm during data collection. X-ray PDF measurements were completed at room temperature at the 11-ID beamline at the APS using a General Electric amorphous Si two-dimensional (2D) detector. The sample to detect or distance was fixed at 117.13 mm, and synchrotron X-rays with the wavelength of 0.2127 Å were utilized with a 0.2 mm×0.2 mm beam size. All other XRD were conducted on an Aeris Research Edition X-ray diffractometer using a Cu target under 40 kV and 15 mA, in the 2θ range of 15−80°. Raman spectroscopy was conducted on WITec alpha300 R Raman microscope. Laser wavelength of 532 nm was applied with a power of 5 mW, a grating of 300 g/mm, and a spectral resolution of 0.1 cm⁻¹ to acquire the Raman data. Each spectrum was collected with 5 scans and 10 s integration for each scan. SEM was conducted on a Zeiss Merlin high-resolution scanning electron microscope. TEM, SAED and EDS were conducted on a JEOL 2010F

transmission electron microscope with an acceleration voltage of 200 kV. Ex situ XANES measurement was conducted at the FXI (18-ID) beamline at the National Synchrotron Light Source II, Brookhaven National Laboratory. High-angle annular dark-field scanning transmission electron microscopy (HAADF-STEM) and electron energy loss spectroscopy (EELS) mapping were performed using the TEAM-1 transmission electron microscope at the National Center for Electron Microscopy, Lawrence Berkeley National Laboratory. This microscope is double aberration-corrected and operates at 300 keV, with a convergence angle of 30 mrad and a beam current of 70 pA. A LASSO filter with thickness effect removal and a turbo colormap were applied to the HAADF-STEM image for better visualization of site occupations. The EELS mapping was acquired using a Gatan GIF Continuum K3 System. During the EELS measurement, the aperture size is 5mm, the dispersion is 0.18 eV/Ch, and the step size is 0.0996 nm. The grain selected for EELS measurement is close to a zone axis such that some lattice fringes can be seen. HAADF-STEM with EDS was performed using Thermo Fisher Scientific Themis Z G3 aberration-corrected scanning transmission electron microscope (STEM) at MIT.Nano, operated at 200 kV with a beam current of 30-40 pA and 19 mrad convergence angle. EDS was collected with a 100 pA beam current on Super-X EDS detectors. XRF was performed on a Bruker Tracer-III SD Portable XRF.

Electrochemical measurements

All electrodes for electrochemical testing were prepared by mixing 70 wt% active material, 20 wt% conductive carbon (Timcal Super C65), and 10 wt% polyvinylidene fluoride (PVDF, Sigma Aldrich) using N-methyl-2-pyrrolidone (NMP, Sigma Aldrich) as the solvent to form a slurry, which was then cast onto an aluminum foil using a 250 μm-gap doctor blade. The loading of the electrode films was 2-3 mg cm^{-1}. A polypropylene (PP, Celgard 2400) membrane was used as the separator. 1.2M LiPF$_6$ dissolved in ethylene carbonate (EC): ethyl methyl carbonate (EMC) = 30:70 wt% solution (Gotion) was used as the electrolyte. Li metal foil was used as the counter and reference electrode. Coin-type cells (CR2032) were assembled in an argon-filled glove box (MBraun). Electrochemical testing of the coin cells was conducted on a Landt CT2001A battery tester (Wuhan Lanhe Electronics) and a Neware battery tester (BTS-9000, Shenzhen, China) at room temperature. Galvanostatic cycling was performed between 1.5 – 4.8 V vs. Li/Li$^+$ at 20 mA g^{-1} for the initial two formation cycles, and then at 50 mA g^{-1} onwards. The rate performance test was performed between 1.5 – 4.8 V vs. Li/Li$^+$ at 20, 50, 200, 500 and 1000 mA g^{-1} for five cycles each, on the same coin cell for each composition. For pouch cells, cathode film with active material loading of 2.5 mg cm^{-1} and dimension of 3 cm × 4 cm was used, paired with Li metal foil. The electrolyte, separator, and galvanostatic cycling test conditions were the same as coin cells. For XANES measurement, electrode samples were prepared by

disassembling coin cells that were charged/discharged to a specific voltage, and then rinsed with dimethyl ether (DME) for two minutes. For ICP-OES measurement, electrolyte samples were prepared by disassembling coin cells after a certain number of cycles, and then soak the cycled cathode film in fresh electrolyte for 10 days at room temperature. For ex situ and XRF measurements, cathode and anode films (lithium metal disc) were obtained by disassembling coin cells after a certain number of cycles, and then rinsed with dimethyl ether (DME) for two minutes. In situ DEMS experiments were carried out using a commercial mass spectrometer (Linglu Instruments Co., Ltd. Shanghai). The DEMS cell was assembled with a Swagelok-type cell, where the diameter and mass-loading of electrode disc were 16 mm and 10 mg cm^{-2}, respectively. The assembled cell was connected to the gas path of the mass spectrometer (Pfeiffer, OminiStar GSD 320). The total carrier gas (Ar) was 3 mL min^{-1}, and the flow was 3 mL min^{-1} through the Swagelok cell. The cell was continuously ventilated for 6 h until the baseline was stable and then charged to 4.8 V vs. Li/Li$^+$ at a current density of 15 mA g^{-1}, and held at 4.8 V vs. Li/Li$^+$ for 4 h.

Author contributions

Y.H., Y.D. and J.L. conceived the project. Y.H. synthesized the materials, and conducted XRD, SEM, ICP-OES, and XRF measurements. Y.H., M.Y., S.L., Y.L. and H.J. contributed to electrochemical testing. Y.Y., Y.S., Y.H., and A.P. contributed to sample preparations, data collection, and data processing for HAADF-STEM and EELS. T.L. contributed to high-resolution XRD and PDF measurements. J.C. and C.S. provided suggestions on the STEM-EELS experiment settings. C.O., Y.Y. and Y.S. wrote the denoise code. Y.P. and M.L. contributed to DEMS measurements. B.W. contributed to TEM imaging, SAED, and STEM-EDS. B.W., Z.C., Y.Z., H.J. contributed to Raman measurements. Z.C. and J.X contributed to ICP-MS measurements. L.M. and X.X. contributed to XANES

measurements. W.L., R.M. and C.Y. contributed to XRD Rietveld refinement. Y.H. and Y.D. analyzed the data. Y.H., Y.D. and J.L. wrote the paper. All authors discussed and contributed to the writing.

Competing interests

The authors declare no competing interests.

References

1. Goodenough, J. B. & Kim, Y. Challenges for rechargeable Li batteries. *Chem. Mater.* **22**, 587-603 (2010).
2. Berg, E. J., Villevieille, C., Streich, D., Trabesinger, S. & Novak, P. Rechargeable batteries: grasping for the limits of chemistry. *J. Electrochem. Soc.* **162**, A2468-A2475 (2015).
3. Ahmed, S., Nelson, P. A., Gallagher, K. G., Susarla, N. & Dees, D. W. Cost and energy demand of producing nickel manganese cobalt cathode material for lithium ion batteries. *J. Power Sources* **342**, 733-740 (2017).
4. Hirsh, H. S. et al. Sodium-ion batteries paving the way for grid energy storage. *Adv Energy Mater.* **10**, 202001274 (2020).
5. Lee, J. et al. Unlocking the potential of cation-disordered oxides for rechargeable lithium batteries. *Science* **343**, 519-522 (2014).
6. Clement, R. J., Lun, Z. & Ceder, G. Cation-disordered rocksalt transition metal oxides and oxyfluorides for high energy lithium-ion cathodes. *Energ. Environ. Sci.* **13**, 345-373 (2020).
7. Ji, H. W. et al. Ultrahigh power and energy density in partially ordered lithium-ion cathode materials. *Nat. Energy* **5**, 213-221 (2020).
8. Lee, J. et al. Reversible Mn^{2+}/Mn^{4+} double redox in lithium-excess cathode materials. *Nature* **556**, 185 (2018).
9. Lun, Z. Y. et al. Cation-disordered rocksalt-type high-entropy cathodes for Li-ion batteries. *Nat. Mater.* **20**, 214 (2021).
10. Yabuuchi, N. et al. High-capacity electrode materials for rechargeable lithium batteries: Li_3NbO_4-based system with cation-disordered rocksalt structure. *P. Natl. Acad. Sci.* **112**, 7650-7655 (2015).
11. Wang, R. et al. A disordered rock-salt Li-excess cathode material with high capacity and substantial oxygen redox activity: $Li_{1.25}Nb_{0.25}Mn_{0.5}O_2$. *Electrochem. Commun.* **60**, 70-73 (2015).
12. Xue, W. J. et al. Ultra-high-voltage Ni-rich layered cathodes in practical Li metal batteries enabled by a sulfonamide-based electrolyte. *Nat. Energy* **6**, 495-505 (2021).
13. Zhu, Z. et al. Gradient-morph $LiCoO_2$ single crystals with stabilized energy density above 3400 W h L^{-1}. *Energ. Environ. Sci.* **13**, 1865-1878 (2020).
14. Armstrong, A. R. et al. Demonstrating oxygen loss and associated structural reorganization in the lithium battery cathode $Li[Ni_{0.2}Li_{0.2}Mn_{0.6}]O_2$. *J. Am. Chem. Soc.* **128**, 8694-8698 (2006).
15. Yoon, M. et al. Unveiling nickel chemistry in stabilizing high-voltage cobalt-rich cathodes for lithium-ion batteries. *Adv. Funct. Mater.* **30**, 201907903 (2020).
16. Zhu, Z. et al. Gradient Li-rich oxide cathode particles immunized against oxygen release by a molten salt treatment. *Nat. Energy* **4**, 1049-1058 (2019).
17. Dong, Y., L. Q., Ana Alvarez, Ju Li, I-Wei Chen. Enhanced mobility of cations and anions in the redox state: the polaronium mechanism. *Acta Materialia* **232**, 117941 (2022).

18. Yan, P. F. et al. Injection of oxygen vacancies in the bulk lattice of layered cathodes. *Nat. Nanotechnol.* **14**, 602 (2019).

19. Lee, J. et al. Determining the criticality of Li-excess for disordered-rocksalt Li-ion battery cathodes. *Adv. Energy Mater.* **11**, 2100204 (2021).

20. Hao Li, R. F., Moohyun Woo, Hoda Ahmed, Dong-Hwa Seo, Rahul malik, Jinhyuk Lee. Toward high-energy Mn-based disordered-rocksalt Li-ion cathodes. *Joule* **6**, 53-91 (2022).

21. Lee, E. S. & Manthiram, A. Smart design of lithium-rich layered oxide cathode compositions with suppressed voltage decay. *J. Mater. Chem. A* **2**, 3932-3939 (2014).

22. Christian M. Julien, A. M., Karim Zaghib, Henri Groult. Comparative issues of cathode materials for Li-ion batteries. *Inorganics* **2**, 132-154 (2014).

23. Radin, M. D. et al. Narrowing the gap between theoretical and practical capacities in Li-ion layered oxide cathode materials. *Adv. Energy. Mater.* **7**, 201602888 (2017).

24. Zhang, W. J. Structure and performance of $LiFePO_4$ cathode materials: a review. *J. Power Sources* **196**, 2962-2970 (2011).

25. Manthiram, A. & Goodenough, J. B. Lithium-based polyanion oxide cathodes. *Nat. Energy* **6**, 844-845 (2021).

26. Manthiram, A. A reflection on lithium-ion battery cathode chemistry. *Nat. Commun.* **11**, 1-9 (2020).

27. Sawamura, M. et al. Nanostructured $LiMnO_2$ with Li_3PO_4 integrated at the atomic scale for high-energy electrode materials with reversible anionic redox. *ACS Central Sci.* **6**, 2326-2338 (2020).

28. House, R. A. et al. Superstructure control of first-cycle voltage hysteresis in oxygen-redox cathodes. *Nature* **577**, 502-508 (2020).

29. Sumita, M., Tanaka, Y., Ikeda, M. & Ohno, T. Theoretically Designed Li_3PO_4 (100)/$LiFePO_4$ (010) Coherent electrolyte/cathode interface for all solid-state Li ion secondary batteries. *J. Phys. Chem. C* **119**, 14-22 (2015).

30. Gnewuch, S. & Rodriguez, E. E. Distinguishing the Intrinsic antiferromagnetism in polycrystalline $LiCoPO_4$ and $LiMnPO_4$ olivines. *Inorg. Chem.* **59**, 5883-5895 (2020).

31. Chung, H. T., Myung, S. T., Cho, T. H. & Son, J. T. Lattice parameter as a measure of electrochemical properties of $LiMn_2O_4$. *J. Power Sources* **97**, 454-457 (2001).

32. Tianyi Li, K. C., Ahmed Hashem, Christian M. Julien. Structural and electrochemical properties of the high Ni content spinel $LiNiMnO_4$. *Electrochem* **2**, 95-117 (2021).

33. Akimoto, J. & Gotoh, Y. Single crystal growth, structure and physical property of $LiCoO_2$ and $LiNiO_2$. *Mol. Cryst. Liq. Cryst.* **341**, 947-950 (2000).

34. de Biasi, L. et al. Chemical, structural, and electronic aspects of formation and degradation behavior on different length scales of Ni-rich NCM and Li-rich HE-NCM cathode materials in Li-ion batteries. *Adv. Mater.* **31**, 201900985 (2019).

35. Markevich, E. et al. Raman spectroscopy of carbon-coated $LiCoPO_4$ and $LiFePO_4$ olivines. *J. of Power Sources* **196**, 6433-6439 (2011).

36. Julien, C. M. & Massot, M. Lattice vibrations of materials for lithium rechargeable batteries III. Lithium manganese oxides. *Mat. Sci. Eng. B-Solid* **100**, 69-78 (2003).

37. Wu, J. et al. In situ Raman spectroscopy of $LiFePO_4$: size and morphology dependence during charge and self-discharge. *Nanotechnology* **24**, 424009 (2013).

38. Tang, D. et al. Electrochemical behavior and surface structural change of $LiMn_2O_4$ charged to 5.1 V. *J. Mater. Chem. A* **2**, 14519-14527 (2014).

39. Tang, D. et al. Surface structure evolution of $LiMn_2O_4$ cathode material upon charge/discharge. *Chem.*

Mater. **26**, 3535-3543 (2014).

40. Manceau, A., Marcus, M. A. & Grangeon, S. Determination of Mn valence states in mixed-valent manganates by XANES spectroscopy. *Am. Mineral* **97**, 816-827 (2012).